A novel transplantable model of lung cancer associated tissue loss and disrupted muscle regeneration

Paige C Arneson[1+], Alexandra M Ducharme[1+], Jason D Doles[1*]

[1]Department of Biochemistry and Molecular Biology, Mayo Clinic, Rochester, Minnesota, 55905 USA, Mayo Clinic, Rochester, Minnesota.

[+]These authors contributed equally to this work

*Corresponding author and lead contact

DESCRIPTIVE ABSTRACT

Background: Cancer-associated muscle wasting (CAW), a symptom of cancer cachexia, is associated with approximately 20% of lung cancer deaths, and remains poorly characterized on a mechanistic level. Current animal models for lung cancer-associated cachexia are limited in that they: 1) primarily employ flank transplantation methods, 2) have short survival times not reflective of the patient condition, and 3) are typically performed in young mice not representative of mean patient age. This study investigates a new model for lung cancer-associated cachexia that can address these issues and also implicates muscle regeneration as a contributor to CAW.

Methods: We used tail vein injection as a method to introduce tumor cells that seed primarily in the lungs of mice. Body composition of tumor bearing mice was longitudinally tracked using magnetic resonance imaging (MRI). These data were combined with histological and molecular assessments of skeletal muscle to provide a complete analysis of muscle wasting.

Results: In this new lung CAW model we observed 1) progressive loss in whole body weight, 2) progressive loss of lean and fat mass, 3) a circulating cytokine/inflammatory profile similar to that seen in other models of CAW, 4) histological changes associated with muscle wasting, and 5) molecular changes in muscle that implicate suppression of muscle repair/regeneration. Finally, we show that survival can be extended without lessening CAW by titrating injected cell number.

Conclusions: Overall, this study describes a new model of CAW that could be useful for further studies of lung cancer-associated wasting and accompanying changes in the regenerative capacity of muscle. Additionally, this model addresses many recent concerns with existing models such as immunocompetence, location of tumor, and survival time.

INTRODUCTION

Cancer cachexia is a complex syndrome associated with approximately 20% of lung cancer deaths; a hallmark symptom of cancer cachexia is cancer-associated muscle wasting (CAW) [1, 2]. Although this syndrome is associated with negative patient outcomes, it remains poorly understood on a mechanistic level. Many groups have investigated the inflammatory environment associated with CAW, in particular, inflammatory cytokines such as tumor necrosis factor alpha (TNFα) and interleukin 6 (IL6). Despite considerable time invested in this area, clinical trials targeting the inflammatory microenvironment alone have been unsuccessful [3, 4]. Other groups have focused on the proteolytic environment in muscle, as a potential driver of CAW, implicating both autophagy and ubiquitin-mediated pathways as potential drivers of CAW [5-7]. The current mechanistic understanding of CAW is largely based off of work done in mouse models, most notably the Lewis lung carcinoma (LLC) and C-26 models.

The LLC model of CAW relies on transplantation of LLC1 non-small cell lung cancer cells, derived from C57/B6 mice, into syngeneic, and thus immunocompetent, C57/B6 recipient mice. The LLC model is one of the few syngeneic and reproducible models for lung cancer/lung-cancer associated wasting available today [8]. Most commonly, LLC1 cells are implanted via flank injection, which results in large primary tumors around 7 days post implantation. A second popular model for CAW, the C26 model, was first described in 1990 and utilizes flank injection of colon 26 carcinoma cells [9]. Like the LLC model, this model displays elevated expression of proteasome components, which contribute to loss of muscle mass [10]. The C26 model presents with longer median survival (25 days) than the LLC model [10]. Notably, both the C26 and LLC models share a common weakness in that tumors do not arise in the tumor tissue of origin. Although recent studies have attempted to correct this issue using autochthonous genetically engineered mouse models (GEMMS), their utility and flexibility are limited. For example, in pancreatic cancer, there have been multiple efforts to create CAW models that focus on tumors arising in their

native tissue via either genetic manipulation or orthotopic implantation [11-15]. The benefits and limitations of these models are addressed in more depth in the discussion. Despite these advances in the context of pancreas cancer, lung cancer models have lagged behind. Orthotopic transplantation has been established in rodent models, but requires an invasive surgery [16] [17]. Furthermore, genetic methods to derive orthotopic tumors in lungs require viral delivery of Cre recombinase [18]. Complications arising in both these models are high and prompted us to develop a simple, reproducible, and scalable model of lung CAW.

We identified the need for better models of CAW that met the following criteria: 1) immunocompetent environment, 2) tumors arising in the appropriate/matching tissue of origin, and 3) ability to modulate the timing/duration of wasting. Here, we present studies on a novel mouse model for lung CAW, which has met these criteria. This model utilizes syngeneic, immunocompetent mice and tail-vein injection of cells as a modality for lung tumor seeding; shows a median survival of approximately 26 days that can be modulated as a function of injected cell number; and exhibits hallmarks of lung CAW. The model presented herein fills a gap in models for studying CAW, and will be a valuable resource for the wasting community moving forward.

RESULTS

Development of a transplantable model for lung cancer-associated tissue loss

Given the increasing need in the CAW field for models featuring tumors arising in their natural location, we sought to develop such a model in the context of lung cancer. To accomplish this, we used tail vein injection as a method whereby injected lung tumor cells implant primarily in the lungs [19]. Cells were derived from a murine lung adenocarcinoma and cultured more than 10 passages prior to injection. Cells were suspended in PBS for the injection and control animals were injected with PBS vehicle only. Throughout the course of the study we assessed body composition via magnetic resonance imaging (MRI) until humane endpoint (see experimental schematic in **Figure 1A**). We performed survival studies on 3 cohorts of mice (total n=10 vehicle and 15 tumor) and observed significantly decreased survival for tumor bearing mice (average survival tumor=26.2 days) (**Figure 1B**). Upon macroscopic inspection of the lungs, tumor bearing mice had many small nodules, fibrotic tissue, and increased tissue density (**Figure 1C**). Upon microscopic inspection of the lungs in tumor-bearing mice, alveolar fields were replaced by multiple, coalescing tumor nodules (>70% in 3 animals, 40-50% in 2 animals assessed). The tumor nodules consisted of loosely packed, vacuolated cells and in some cases were associated with small clusters of intra-tumoral lymphocytes, usually at the margins of blood vessels or nodules. Lastly, the pleural surface was roughened by projecting fronds / plaques of tumor cells. In comparison, vehicle animals displayed expanded alveolar spaces and a smooth pleural surface (**Figure 1D**). Furthermore, we observed a statistically significant increase in total lung weight in tumor-bearing mice (**Figure 1E**).

Concurrent with evaluations of tumor effects on overall survival, we performed longitudinal body composition analyses. First, we observed a significant difference in time and treatment co-variance for body weight, which was highlighted by significant decreases in body weight at 10, 14, and 17 days post tumor implantation (**Figure 1F**). Next, we observed a significant difference in time and treatment co-variance for total fat mass, which was highlighted by significant

107 decreases in fat mass at 14, 17, and 21 days post tumor implantation (**Figure**
108 **1G**). Lastly, we observed a significant difference in time and group co-variance in
109 total lean mass, although individual days had no significant difference (**Figure**
110 **1H**). Overall, there were decreases in total body weight, total fat mass, and total
111 lean mass as the tumor progressed (the latter two measured by MRI) (**Figure 1F-**
112 **H**).

113 Lung cancer-associated inflammation

114 Loss in both body weight and lean mass are hallmarks of CAW. Many studies
115 have implicated heightened inflammatory signaling as a driver of CAW [20-22].
116 We quantitatively assessed concentrations of 31 cytokines in the serum of tumor-
117 bearing and vehicle animals (EveTechnologies) (n=5 vehicle and 4 tumor).
118 Ranked analysis (vertically by their average in the tumor-bearing animals;
119 highest to lowest) revealed substantial differences between experimental groups
120 (**Figure 2A).** Specifically, we observed significant differences in 4 factors:
121 Eotaxin (down~2 fold), C-X-C motif chemokine 5 (LIX, down ~10 fold), TNFα (up
122 ~30 fold) and vascular endothelial growth factor (VEGF, up ~190 fold) (**Figure**
123 **2C**). Of note, TNFα accumulation has been previously implicated in CAW [20,
124 23].

125 Lung cancer-associated muscle loss

126 Considering both the loss of lean mass by MRI analysis and the accumulation of
127 classical markers of CAW in the serum, we next performed a histological and
128 molecular assessment of skeletal muscle. First, we assessed tibialis anterior (TA)
129 muscle cross sections by immunofluorescent staining for laminin, a marker of
130 myofiber membranes, and DAPI (nuclei) (**Figure 3A**). Minimum feret diameters
131 were measured, compiled, and calculated using myovision (mean feret diameter:
132 3 million = 40.4 um, vehicle = 44.4 um, and found a statistically significant
133 decrease in the non-linear regressions fit to the histograms of minimum feret
134 diameter distribution of tumor-bearing mice(**Figure 3B**) [24]. Additionally, we
135 observed a significant decrease in TA weight in tumor bearing animals; this was
136 not due to a reduction in the total number of myofibers in the TA of these animals

137 (**Figure 3C-D**). Since we observed a reduction in myofiber size, but not total
138 number of myofibers, we postulated that this could be due to a decrease in the
139 regenerative capacity of muscle. Using immunofluorescent staining, we queried
140 the number of Pax7 positive muscle progenitor cells. We observed a statistically
141 significant increase in Pax7 positive cells per millimeter squared of tissue (**Figure**
142 **3E**). Additionally, we assessed the number of centrally located nuclei (CLN),
143 which mark actively regenerating myofibers containing recently fused muscle
144 progenitor cells. We did not see any difference in the number of CLN per
145 millimeter squared of tissue between vehicle and tumor-bearing mice (**Figure**
146 **3F**). Lastly, to acquire a molecular understanding of regenerative capacity of
147 muscle from tumor-bearing animals, we used quantitative RT-PCR to measure
148 several transcripts associated with early myogenesis, late myogenesis/fusion,
149 and muscle atrophy. Visualized in a heat map, we see a trend toward higher
150 expression of atrophy transcripts (Trim63 and Fbxo32) and early makers of
151 myogenesis (Pax7 and Myod1), and lower expression of late markers of
152 myogenesis (**Figure 3G**).

153 <u>Transplanted cell number correlates with survival and CAW progression</u>

154 Upon establishing that our lung cancer model induces loss in total body weight,
155 lean mass, and is also associated with an impaired muscle regeneration
156 phenotype, we sought to determine if survival time/CAW progression could be
157 experimentally modulated. To accomplish this, we varied the number of cells
158 injected as follows: 3 million cells (used in all previous figures), 1 million cells,
159 300,000 cells, and vehicle. We also tested 30,000 and 3,000 cells but found
160 inconsistent inoculation of tumors and omitted these groups from further study
161 (data not shown). We assessed survival of animals in each group and found that
162 lowering the number of cells injected prolonged survival as evidenced by a
163 statistical increase in survival from 3 million to 1 million cells ($p=0.0208$), 1 million
164 to 300,000 cells ($p=0.0024$), and 300,000 cells to vehicle ($p=0.0046$) (**Figure 4A-**
165 **B)**. We also observed changes in lung condition, as evidenced by increased lung
166 weight in 3 and 1 million injected cells, and macroscopic changes in lung
167 condition similar to those observed previously (**Figure 4C-D**).

168 We next performed body composition and muscle morphometrics analyses in
169 mice receiving variable numbers of tumor cells. As before, we observed
170 decreasing trends in body mass, lean mass and fat mass in tumor bearing mice
171 of all groups (**Figure 5A-C**). Specifically, we observed significant difference in
172 time and treatment co-variance for body weight, in 3 million, 1 million, and
173 300,000 implanted cell groups compared to vehicle (**Figure 5A**). We also
174 observed significant difference in time and treatment co-variance for total lean
175 mass in 3 million and 1 million implanted cell groups compared to vehicle (**Figure**
176 **5B**). In lower implantation doses, we did not observe significant differences in
177 total fat mass. Because tumors were restricted primarily to the lungs (with the
178 exception of some metastases) (**Table 1**), it was not possible to discount tumor
179 mass from MRI measurements. Evaluation of TA muscles from tumor-bearing
180 mice revealed statistically decreases in TA mass in the 300,000 cells group,
181 similar to the 3 million cells group (**Figure 5D**). Additionally, myovision-based
182 assessment of minimum feret diameters revealed increasingly significant
183 decreases as the cell injection number decreased (mean feret diameter: 1 million
184 = 41.3 um, 300,000 = 32.6 um, vehicle = 44.4 um)(**Figure 5E**).

185

186 **DISCUSSION**

187 In order to gain a more thorough understanding of CAW, there is a need for
188 models that more accurately capture the patient condition. This new and novel
189 model for CAW meets several needs in the field such as: 1) immunocompetence
190 (i.e. a syngeneic model), 2) exhibits both heightened catabolism and suppressed
191 regeneration 3) exhibits both lean and fat mass loss, 4) exhibits an inflammatory
192 microenvironment, 5) is flexible in timing and severity, 6) arises in the tumor's
193 organ of origin. To the last point, recent studies have highlighted the importance
194 of tumor location on both tumor development and CAW [25-27]. Our model is an
195 easy and effective method to induce tumor formation in the lungs and
196 concomitant CAW, using lung adenocarcinoma cells.

197 With regard to points two through four, developing therapeutics for CAW is
198 ultimately dependent on mouse models that reflect the complex molecular nature
199 of this syndrome. We showed that this model exhibits an inflammatory signature
200 similar to published signatures of CAW patients [20, 21, 28-30]. Additionally, our
201 model supports numerous studies linking both elevated catabolism and impaired
202 skeletal muscle regeneration as contributors to CAW [5-7, 31]. Our observation
203 that there is an accumulation of Pax7+ cells in the TA muscle, but no change in
204 the number of centrally located nuclei may be indicative of increased progenitor
205 cell expansion, with failure to incorporate into the damaged/cachectic muscle.
206 Although we probed genes related to fusion and progenitor cell maturation by
207 qPCR and did not observe differences in expression, a more detailed
208 assessment of the progenitor cell population would be necessary to make
209 definitive conclusions about suppressed muscle regeneration in this model.

210 A major weakness of many CAW mouse models is the age of wasting onset.
211 Genetic models, such as the KPC model, are predisposed to spontaneously
212 develop tumors, which gives investigators little control over the age of onset.
213 With cachectic cancers affecting a primarily elderly population, it is critical that
214 new models are able to account for this confounding factor. For pancreatic
215 cancer, this problem has largely been solved by the KPP mouse, which

216 expresses pancreas-specific oncogenes under Cre recombinase control [13].
217 However, for lung cancer, this is only beginning to be addressed[15]. Although
218 our model has not yet been adapted for use in aged mice, the transplantable
219 nature of the model permits use in any age of animal. Our model has the added
220 attraction that it does not require a major surgery or viral infection, which could
221 affect inflammatory status, making it more amenable for aged animals with higher
222 frailty than young animals [32].

223 The lack of CAW models that accurately assess the effects of age highlights a
224 second issue, which is the difference between muscle atrophy and the absence
225 of growth. A primary concern with the KPC pancreatic cancer mouse model is
226 that these mice are significantly smaller than littermate controls prior to palpable
227 tumor development. This suggests that fetal expression of the oncogenes is
228 contributing to impaired muscle development [13]. Although spontaneous genetic
229 models, such as the KPC model, are dramatic examples of the difference
230 between atrophy and absence of growth, this principle implicates many
231 transplantation models [33]. Even in the study presented here, with age-matched
232 controls, it is evident that mice in the 3-6 month age group are still growing
233 (gaining total body weight and fat mass). Although muscle development is
234 typically considered complete at 3 months and lean mass is essentially stabilized
235 in our animals, this anabolic state is unrepresentative of the patient population
236 [13, 34, 35]. The model presented here is amenable to assessing CAW in aged
237 animals (greater than one year), which may lead to a better understanding of
238 CAW mechanisms and more efficient translatability to the clinic.

239 Another aspect of the patient condition poorly modeled in rodents is the severity
240 and duration of wasting symptoms. Recently, it was established that the cachexia
241 syndrome could be divided into three clinical stages: pre-cachexia, cachexia, and
242 refractory cachexia. Although refractory cachexia is marked by a short (only three
243 months) survival, wasting is present for much longer – an important observation
244 that is difficult to study in rapidly progressing rodent CAW models. Importantly,
245 with respect to intervention, some suggest that it is in the earlier stages (non-
246 refractory) that therapeutics may be more effective [36]. Despite these features in

247 patients, mouse models like LLC and C26 have rapid symptom onset and short
248 survival times. Failing to capture the earlier stages of cachexia is likely a
249 contributor to the failed clinical trials based on pre-clinical data derived using
250 these models. The ability of our model to be titrated by cell dosage provides an
251 important opportunity explore the timing and duration of wasting symptoms more
252 thoroughly.

253 Despite the many strengths highlighted in this study, the model presented herein
254 does have limitations. Perhaps the most notable limitation is one common to all
255 orthotopic lung cancer models, which is the difficulty for assessing tumor burden
256 in living animals. This could be remediated by stably transfecting cells with a
257 fluorescent reporter and utilizing *in vivo* imaging modalities. Additionally, in some
258 cohorts, we observed high levels of metastasis outside the thoracic cavity. This
259 may be representative of patients that exhibit metastases, but also complicates
260 data interpretation. Nevertheless, the model presented here is an important step
261 forward as CAW research progresses and will be a valuable resource for future
262 research aimed at understanding the etiology of lung cancer-associated muscle
263 and fat wasting.

264

ACKNOWLEDGEMENTS

The authors wish to thank members of the Doles lab for helpful discussions and manuscript suggestions. Additionally, the authors extend thanks to Brad Bolon, DVM, MS, PhD of GEMpath INC for assisting in the pathological analyses. J.D. was supported by the National Institute of Health/National Institute of Arthritis, Musculoskeletal and Skin Diseases (NIH/NIAMS) R00AR66696, Mayo Clinic start-up funds, Career Development Awards from the Mayo Clinic SPORE in Pancreatic Cancer (NIH/ National Cancer Institute (NCI) CA102701) and the American Association for Cancer Research/Pancreatic Cancer Action Network. P.C.A was supported by the Mayo Clinic Regenerative Sciences Training Program (RSTP).

AUTHOR CONTRIBUTIONS

Study design: JDD, PCA, AMD. Data collection: PCA and AMD. Data analysis/interpretation: JDD, PCA, AMD. Writing and editing of manuscript: JDD, PCA, AMD. All authors approved this manuscript.

COMPETING INTERESTS STATEMENT

The authors have no competing interests to declare.

282 **FIGURE LEGENDS**

283 **Figure 1: Transplantable model for lung cancer-associated tissue loss. (A)**
284 Schematic of the study design. D0 = day tumor cells were injected into mice. All
285 studies were survival studies, so endpoint was variable, but the median survival
286 was 26 days. MRI scans were completed twice per week during the course of the
287 study. **(B)** Survival curve for vehicle and tumor injected cells. Dotted vertical line
288 indicates the median survival (26 days). N- 10 vehicle, 15 tumor. Data were
289 compiled from 3 independent cohorts of animals. Survival is statistically different
290 ($p<0.0001$) by Gehan-Breslow-Wilcoxon test. (**C)** Representative images of
291 lungs from vehicle and tumor bearing mice. Ruler reference in centimeters. **(D)**
292 Representative hematoxylin and eosin (H&E) staining of lung tissue from vehicle
293 (left) and tumor bearing (right) mice. 2 representative images from 2 individual
294 animals in each condition. Scale bar is 800 um. **(E)** Total lung weight (all lobes)
295 from vehicle and tumor-bearing mice. Individual points represent individual
296 animals. Boxes represent the inner quartiles and whiskers represent the
297 minimum and maximum values. **(F)** Total mouse weight across study, normalized
298 to pre-tumor baseline weight. Error bars are SEM. p values presented in the
299 figure are the result of mixed-effects analysis, with Geisser-Greenhouse
300 correction. Significance at individual points was determined by correction for
301 multiple testing using false discovery rate (Benjamini and Hochberg). **(G)** MRI
302 calculated total fat mass across study, normalized to pre-tumor baseline fat
303 mass. Error bars are SEM, statistical analysis is as described above. **(H)** MRI
304 calculated total lean mass across study, normalized to pre-tumor baseline lean
305 mass. Error bars are SEM, statistical analysis is as described above. *$p<0.05$ by
306 student's t test n= 5 vehicle, 4 tumor-bearing 7-week-old male 129S2/SvPasCrl
307 mice for all data except survival curve.

308

309 **Figure 2: Lung cancer-associated inflammation. (A)** Heat map of 29 cytokines
310 profiled in the serum of vehicle or tumor-bearing mice. Features are sorted by the
311 highest average of the tumor samples, from top to bottom. Values are the

312 concentration, row normalized for each feature, then log2 transformed. Red =
313 high expression, Blue = low expression. **(B)** Bar graph of cytokines commonly
314 associated with muscle wasting and/or cancer cachexia. Individual points
315 represent individual animals. Boxes represent the inner quartile and whiskers
316 represent the minimum and maximum values. **(C)** Bar graph of cytokines
317 significantly upregulated in tumor bearing animals. Individual points represent
318 individual animals. Boxes represent the inner quartile and whiskers represent the
319 minimum and maximum values. *$p<0.05$ in multiple t test with Holm-Sidak
320 multiple testing correction. n= 5 vehicle, 4 tumor-bearing 7-week-old male
321 129S2/SvPasCrl mice.

322

323 **Figure 3: Lung cancer-associated muscle loss. (A)** Representative images of
324 vehicle (left two images) and tumor-bearing (right two images) tibialis anterior
325 (TA) muscle cross sections. Immunofluorescent staining for Laminin (myofiber
326 membranes, white) and DAPI (nuclei, blue). **(B)** Quantification of minimum feret
327 diameters of myofibers from tumor-bearing and vehicle mice. Feret diameters
328 were binned to a histogram and fit with a non-linear regression (gaussian, least
329 squares regression). Myofibers of tumor-bearing animals were significantly
330 smaller than vehicle; $p=0.0142$. **(C)** Wet weight of TA muscle from vehicle and
331 tumor-bearing animals. Individual points represent individual animals. Boxes
332 represent the inner quartile and whiskers represent the minimum and maximum
333 values. **(D)** Wet weight of gastrocnemius (GR) muscle from vehicle and tumor-
334 bearing animals. Individual points represent individual animals. Boxes represent
335 the inner quartile and whiskers represent the minimum and maximum values. **(E)**
336 Quantification of Pax7 positive cells per millimeter squared in TA cross sections
337 of vehicle or tumor-bearing animals. Individual points represent individual
338 animals. Boxes represent the inner quartile and whiskers represent the minimum
339 and maximum values. **(F)** Quantification of centrally located nuclei per myofiber
340 in TA cross sections. Individual points represent individual animals. Boxes
341 represent the inner quartile and whiskers represent the minimum and maximum
342 values. **(G)** Heat map depicting 16 transcripts assessed by qPCR in

343 gastrocnemius muscle of vehicle or tumor-bearing animals. Transcripts are
344 sorted by highest expression average of tumor sample from top to bottom.
345 Orange = high expression, Blue = low expression. *P<0.05 by student's t test n=
346 5, 7-week-old male 129S2/SvPasCrl mice for each group.

347

348 **Figure 4: Tumor cell number titration modulates survival time. (A)** Survival
349 curve for mice injected with vehicle or a range of tumor cells (300,000, 1 million,
350 or 3 million). **(B)** Table depicting the median survival for each group. **(C)** Total
351 lung weight (all lobes) in milligrams for each group. Individual points represent
352 individual animals. Boxes represent the inner quartile and whiskers represent the
353 minimum and maximum values. *p<0.05 student's t test. n= 5, vehicle; 4, 3-
354 million; 5, 1-million; 3, 300,000 7-week-old male 129S2/SvPasCrl mice. **(D)**
355 Representative images of lungs from vehicle, 300,000 cells and 3 million cells
356 groups. Ruler reference is in centimeters.

357

358 **Figure 5: Tumor-bearing mice exhibit progressive tissue loss regardless of**
359 **initial transplanted cell number. (A)** Total mouse weight across study,
360 normalized to pre-tumor baseline weight. Error bars are SEM, statistical analysis
361 is as described in 1F. **(B)** MRI calculated total fat mass across study, normalized
362 to pre-tumor baseline fat mass. Error bars are SEM, statistical analysis is as
363 described in 1F. **(C)** MRI calculated total lean mass across study, normalized to
364 pre-tumor baseline lean mass. Error bars are SEM, statistical analysis is as
365 described in 1F. **(D)** TA weight in milligrams for each group in study. Individual
366 points represent individual animals. Boxes represent the inner quartile and
367 whiskers represent the minimum and maximum values. **(E)** Quantification of
368 minimum feret diameters from muscles of tumor-bearing (1 million cells or
369 300,000 cells) and vehicle-treated mice. Feret diameters were binned to a
370 histogram and fit with a non-linear regression (gaussian, least squares
371 regression). Myofibers from tumor-bearing mice were smaller, p values
372 calculated by extra sun-of-squares F test. 1 million vs. vehicle (left, p= 0.0523),

373 300,000 vs. vehicle (right, $p<0.0001$). n= 5, vehicle; 4, 3-million; 5, 1-million; 3,
374 300,000 7-week-old male 129S2/SvPasCrl mice.

375

376 **Table 1: Metastatic characteristics of 393P lung cancer-associated wasting**
377 **model.** Percentage of animals bearing nodular tumors visible with the naked eye
378 during necropsy and qualitative assessment of necropsied animals showing
379 metastases in the thorax, lower back, and upper hindlimb regions.

380

381

382 **METHODS**

383 **Animals**

384 Mice were bred and housed according to NIH guidelines for the ethical treatment
385 of animals in a pathogen-free facility at the Mayo Clinic (Rochester, MN campus).
386 Mayo Clinic's Institutional Animal Care and Use Committee (IACUC) approved all
387 animal protocols. For 393P-induced CAW model, 150 uL 393P cells (containing
388 3×10^6, 1×10^6, or 3×10^5 cells depending on group), or an equal volume of PBS
389 (Gibco, 14190-144) (control) was injected via tail vein into 7-week-old male
390 129S2/SvPasCrl mice (Jackson Laboratories, Bar Harbor, ME). Development of
391 cachexia was monitored twice weekly by body weight, fat, and lean mass. Mice
392 were euthanized when endpoint criteria (weight loss greater than or equal to 20%
393 of body weight, inability to ambulate, inability to reach food and/or water, tumors
394 greater than or equal to 10% of body weight, tumors that have ulcerated, a body
395 condition score of 1 or less using the IACUC approved scoring system) was
396 reached. Blood serum, heart muscle, lungs, tibialis anterior (TA), gastrocnemius
397 (GR) and epididymal fat pad were collected immediately for analyses. Exact n for
398 each experiment included in the figure legends.

399 **Animal imaging**

400 Body weight, lean mass, and fat mass were measured twice weekly until
401 endpoint. A baseline measurement was taken prior to start of study. Body
402 composition was measured using magnetic resonance imaging (EchoMRI-
403 100/130) system, EchoMRI, Houston, TX, USA).

404 **Cell culture**

405 393P cells were grown on tissue culture treated dishes in growth media
406 consisting of DMEM media (Gibco #11995-065, lot 2051518) supplemented with
407 10% fetal bovine serum (Gibco #10099131, lot 2017488) and antibiotics. Cells
408 were validated by IDEXX analytics and confirmed to be a pure culture and

409 murine in origin. Cells were removed from plate with TrypLE (Gibco, 12604-013),
410 counted, and resuspended in PBS prior to injection.

411 **Immunostaining**

412 Left TA whole muscle was prepared for O.C.T embedding and cryosectioned.
413 Tissue sections (8-10um) were post-fixed in 4% paraformaldehyde for 5 minutes
414 at room temperature prior to immunostaining. Once fixed, isolated tissue
415 sections were permeabilized with 0.5% Triton-X100 in PBS, followed by blocking
416 with 3% BSA in PBS. Primary antibody incubations occurred at RT for 90
417 minutes or overnight in 4 degrees, and secondary antibody incubations followed
418 at RT for 45 minutes in 3% BSA in PBS. The following antibodies were used in
419 this study: Laminin (Sigma 4HB-2) and Pax7 (developmental hybridoma bank).
420 Secondary antibodies were all Alexa fluorescent conjugates (488, 555, or 647)
421 from Invitrogen or Jackson ImmunoResearch. Stained tissue sections were
422 imaged on a (Nikon Eclipse Ti-U camera and microscope system). Acquired
423 images were analyzed for myofiber feret diameters using myovison and manual
424 colocalization quantification using ImageJ.

425 **Cytokine Studies**

426 Blood serum was collected from mice at endpoint. The MD31 cytokine panel was
427 performed by Eve Technologies (Eve Technologies, Calgary, AB Canada) and
428 samples were prepared as recommended by Eve Technologies. All samples
429 were run in technical duplicate.

430 **Q-PCR**

431 Total gastrocnemius RNA was isolated, purified, and DNase I treated using Trizol
432 and purified on RNeasy Mini kit columns (Qiagen, Mississauga, ON, Canada).
433 RNA was quantified using a NanoDrop Spectrophotometer (ThermoScientific,
434 Wilmington, DE, USA). Two ug of total RNA was reverse transcribed with
435 primers using the High-Capacity cDNA Reverse Transcription Kit (Life
436 Technologies, Carlsbad, CA, USA). QPCR was performed on a ViiA7

437 Quantitative PCR System (Applied Biosystems by Life Technologies, Austin, TX,
438 USA). All samples were run in technical triplicate. Standard delta delta CT
439 analysis was used post PCR. Primer sequences are available upon request.

440 **Lung, Heart and TA Histopathology**

441 At endpoint lung, heart and right TA whole muscle were fixed in 4%
442 paraformaldehyde. After 24 hours, tissue was moved to 70% ethanol. Tissue
443 was embedded in paraffin and tissue sections (6 um) were incubated at 37
444 degrees for 60 minutes prior to staining with hematoxylin and eosin (H&E).
445 Stained tissue sections were analyzed by GEMpath Inc. (Dr. Brad Bolon,
446 Longmont, CO) and imaged on a Nikon Eclipse Ts2 microscope. Samples could
447 be segregated with 100% reliability at using both the naked eye and the
448 microscope.

449 **Statistics**

450 Data are represented as the mean ± SD using GraphPad Prism (GraphPad
451 Software, San Diego, CA) unless noted otherwise in the figure legends.
452 Quantification of muscle cross sections using minimum feret diameter
453 measurements was analyzed by non-linear regression (least squares method)
454 and compared between conditions using an extra-sum-of-squares F test. All
455 other comparisons between groups were performed using unpaired two-tailed
456 student's t tests or mixed-effects analysis, as noted in figure legends. For all
457 analyses, a $p<0.05$ was considered significant (denoted with *)

458 **Data availability**

459 Datasets generated during the current study are available from the
460 corresponding author upon request.

461 **REFERENCES**

462 1. Zhu, R., et al., *Updates on the pathogenesis of advanced lung cancer-*
463 *induced cachexia.* Thoracic cancer, 2019. **10**(1): p. 8-16.
464 2. Baracos, V.E., et al., *Body composition in patients with non-small cell lung*
465 *cancer: a contemporary view of cancer cachexia with the use of computed*
466 *tomography image analysis.* Am J Clin Nutr, 2010. **91**(4): p. 1133S-
467 1137S.
468 3. Porporato, P.E., *Understanding cachexia as a cancer metabolism*
469 *syndrome.* Oncogenesis, 2016. **5**: p. e200.
470 4. Jatoi, A., et al., *A placebo-controlled, double-blind trial of infliximab for*
471 *cancer-associated weight loss in elderly and/or poor performance non-*
472 *small cell lung cancer patients (N01C9).* Lung Cancer, 2010. **68**(2): p.
473 234-9.
474 5. Pettersen, K., et al., *Cancer cachexia associates with a systemic*
475 *autophagy-inducing activity mimicked by cancer cell-derived IL-6 trans-*
476 *signaling.* Sci Rep, 2017. **7**(1): p. 2046.
477 6. Yuan, L., et al., *Muscle-specific E3 ubiquitin ligases are involved in muscle*
478 *atrophy of cancer cachexia: an in vitro and in vivo study.* Oncol Rep,
479 2015. **33**(5): p. 2261-8.
480 7. Baracos, V.E., et al., *Activation of the ATP-ubiquitin-proteasome pathway*
481 *in skeletal muscle of cachectic rats bearing a hepatoma.* Am J Physiol,
482 1995. **268**(5 Pt 1): p. E996-1006.
483 8. Kellar, A., C. Egan, and D. Morris, *Preclinical Murine Models for Lung*
484 *Cancer: Clinical Trial Applications.* Biomed Res Int, 2015. **2015**: p.
485 621324.
486 9. Tanaka, Y., et al., *Experimental cancer cachexia induced by*
487 *transplantable colon 26 adenocarcinoma in mice.* Cancer Res, 1990.
488 **50**(8): p. 2290-5.
489 10. Aulino, P., et al., *Molecular, cellular and physiological characterization of*
490 *the cancer cachexia-inducing C26 colon carcinoma in mouse.* BMC
491 Cancer, 2010. **10**: p. 363.
492 11. Lewis, B.C., D.S. Klimstra, and H.E. Varmus, *The c-myc and PyMT*
493 *oncogenes induce different tumor types in a somatic mouse model for*
494 *pancreatic cancer.* Genes & development, 2003. **17**(24): p. 3127-3138.
495 12. Shukla, S.K., et al., *Silibinin-mediated metabolic reprogramming*
496 *attenuates pancreatic cancer-induced cachexia and tumor growth.*
497 Oncotarget, 2015. **6**(38): p. 41146.
498 13. Talbert, E.E., et al., *Modeling Human Cancer-induced Cachexia.* Cell Rep,
499 2019. **28**(6): p. 1612-1622 e4.
500 14. Frese, K.K. and D.A. Tuveson, *Maximizing mouse cancer models.* Nature
501 Reviews Cancer, 2007. **7**(9): p. 654.
502 15. Goncalves, M.D., et al., *Fenofibrate prevents skeletal muscle loss in mice*
503 *with lung cancer.* Proceedings of the National Academy of Sciences,
504 2018. **115**(4): p. E743-E752.

16. Fujiwara, T., et al., *Therapeutic Effect of a Retroviral Wild-Type p53 Expression Vector in an Orthotopic Lung Cancer Model.* JNCI: Journal of the National Cancer Institute, 1994. **86**(19): p. 1458-1462.
17. Howard, R.B., et al., *Characterization of a highly metastatic, orthotopic lung cancer model in the nude rat.* Clinical & experimental metastasis, 1999. **17**(2): p. 157-162.
18. DuPage, M., A.L. Dooley, and T. Jacks, *Conditional mouse lung cancer models using adenoviral or lentiviral delivery of Cre recombinase.* Nat Protoc, 2009. **4**(7): p. 1064-72.
19. Doles, J., et al., *Suppression of Rev3, the catalytic subunit of Pol{zeta}, sensitizes drug-resistant lung tumors to chemotherapy.* Proc Natl Acad Sci U S A, 2010. **107**(48): p. 20786-91.
20. Ma, J.F., et al., *STAT3 promotes IFNγ/TNFα-induced muscle wasting in an NF-κB-dependent and IL-6-independent manner.* EMBO Mol Med, 2017. **9**(5): p. 622-637.
21. Zimmers, T.A., M.L. Fishel, and A. Bonetto, *STAT3 in the systemic inflammation of cancer cachexia.* Semin Cell Dev Biol, 2016. **54**: p. 28-41.
22. Hogan, K.A., et al., *Tumor-derived cytokines impair myogenesis and alter the skeletal muscle immune microenvironment.* Cytokine, 2017.
23. Magee, P., S. Pearson, and J. Allen, *The omega-3 fatty acid, eicosapentaenoic acid (EPA), prevents the damaging effects of tumour necrosis factor (TNF)-alpha during murine skeletal muscle cell differentiation.* Lipids Health Dis, 2008. **7**: p. 24.
24. Wen, Y., et al., *MyoVision: software for automated high-content analysis of skeletal muscle immunohistochemistry.* J Appl Physiol (1985), 2018. **124**(1): p. 40-51.
25. Muir, A., L.V. Danai, and M.G. Vander Heiden, *Microenvironmental regulation of cancer cell metabolism: implications for experimental design and translational studies.* Dis Model Mech, 2018. **11**(8).
26. Yanagihara, K., et al., *Development and characterization of a cancer cachexia model employing a rare human duodenal neuroendocrine carcinoma-originating cell line.* Oncotarget, 2019. **10**(25): p. 2435.
27. Erstad, D.J., et al., *Orthotopic and heterotopic murine models of pancreatic cancer and their different responses to FOLFIRINOX chemotherapy.* Disease models & mechanisms, 2018. **11**(7): p. dmm034793.
28. Horikawa, N., et al., *Expression of vascular endothelial growth factor in ovarian cancer inhibits tumor immunity through the accumulation of myeloid-derived suppressor cells.* Clinical Cancer Research, 2017. **23**(2): p. 587-599.
29. Tachibana, K., et al., *IL-17 and VEGF are increased and correlated to systemic inflammation, immune suppression, and malnutrition in patients with breast cancer.* European Journal of Inflammation, 2017. **15**(3): p. 219-228.

549 30. Gelin, J., et al., *Role of endogenous tumor necrosis factor alpha and*
550 *interleukin 1 for experimental tumor growth and the development of cancer*
551 *cachexia.* Cancer Res, 1991. **51**(1): p. 415-21.
552 31. He, W.A., et al., *NF-κB-mediated Pax7 dysregulation in the muscle*
553 *microenvironment promotes cancer cachexia.* J Clin Invest, 2013.
554 **123**(11): p. 4821-35.
555 32. Pfeifer, A. and I.M. Verma, *Gene therapy: promises and problems.* Annual
556 review of genomics and human genetics, 2001. **2**(1): p. 177-211.
557 33. White, R.B., et al., *Dynamics of muscle fibre growth during postnatal*
558 *mouse development.* BMC developmental biology, 2010. **10**(1): p. 21.
559 34. Aoki, T., et al., *Evolution of peripheral lung adenocarcinomas: CT findings*
560 *correlated with histology and tumor doubling time.* American journal of
561 roentgenology, 2000. **174**(3): p. 763-768.
562 35. Zhang, Y., et al., *Frequency of driver mutations in lung adenocarcinoma*
563 *from female never-smokers varies with histologic subtypes and age at*
564 *diagnosis.* Clinical cancer research, 2012. **18**(7): p. 1947-1953.
565 36. Fearon, K., et al., *Definition and classification of cancer cachexia: an*
566 *international consensus.* Lancet Oncol, 2011. **12**(5): p. 489-95.
567

Figure 1

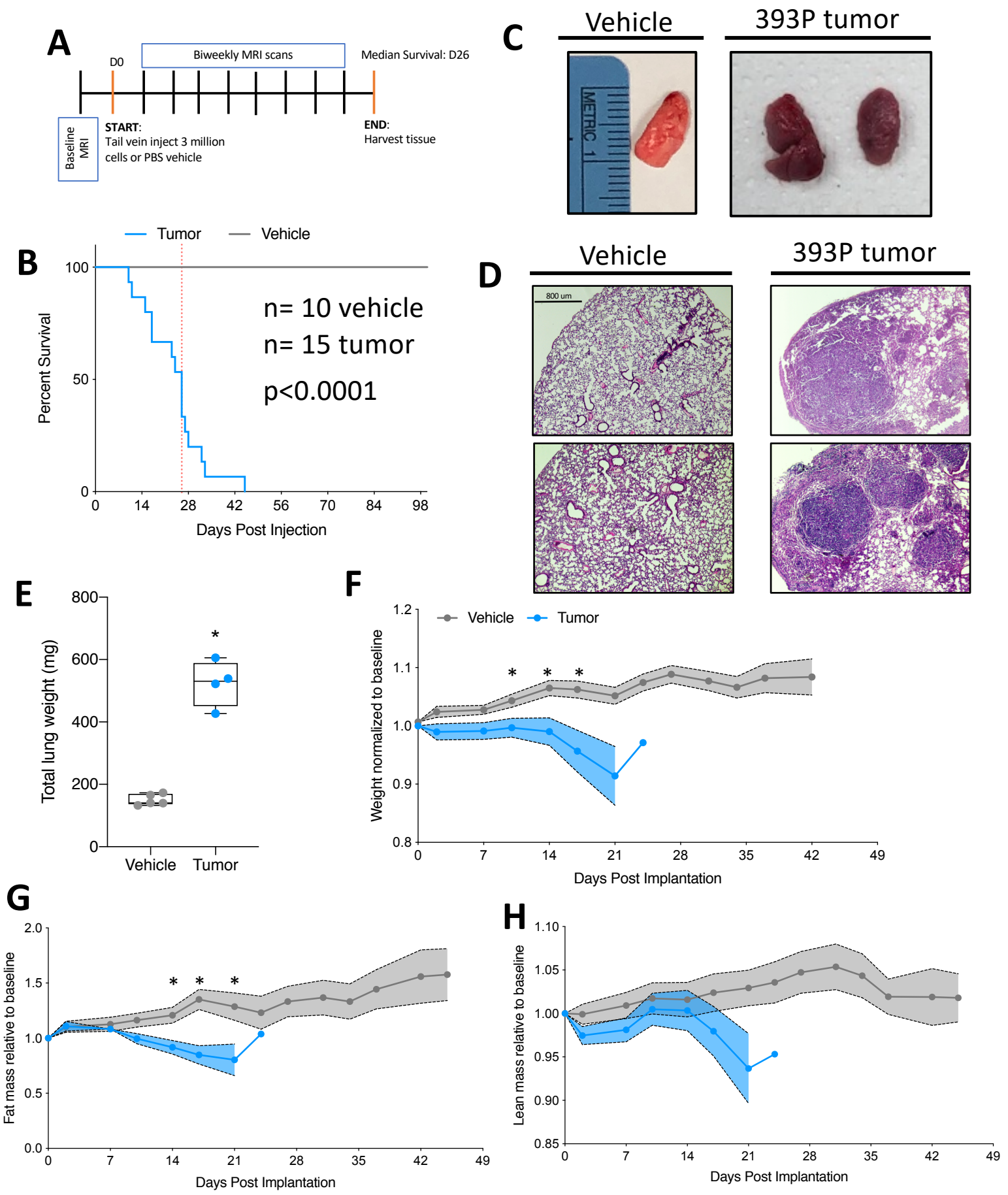
A
D0
Biweekly MRI scans
Median Survival: D26
Baseline MRI
START:
Tail vein inject 3 million cells or PBS vehicle
END:
Harvest tissue
B
Tumor
Vehicle
Percent Survival
Days Post Injection
n= 10 vehicle
n= 15 tumor
p<0.0001
C
Vehicle
393P tumor
D
Vehicle
393P tumor
800 um
E
Total lung weight (mg)
Vehicle
Tumor
F
Vehicle
Tumor
Weight normalized to baseline
Days Post Implantation
G
Fat mass relative to baseline
Days Post Implantation
H
Lean mass relative to baseline
Days Post Implantation

Figure 2

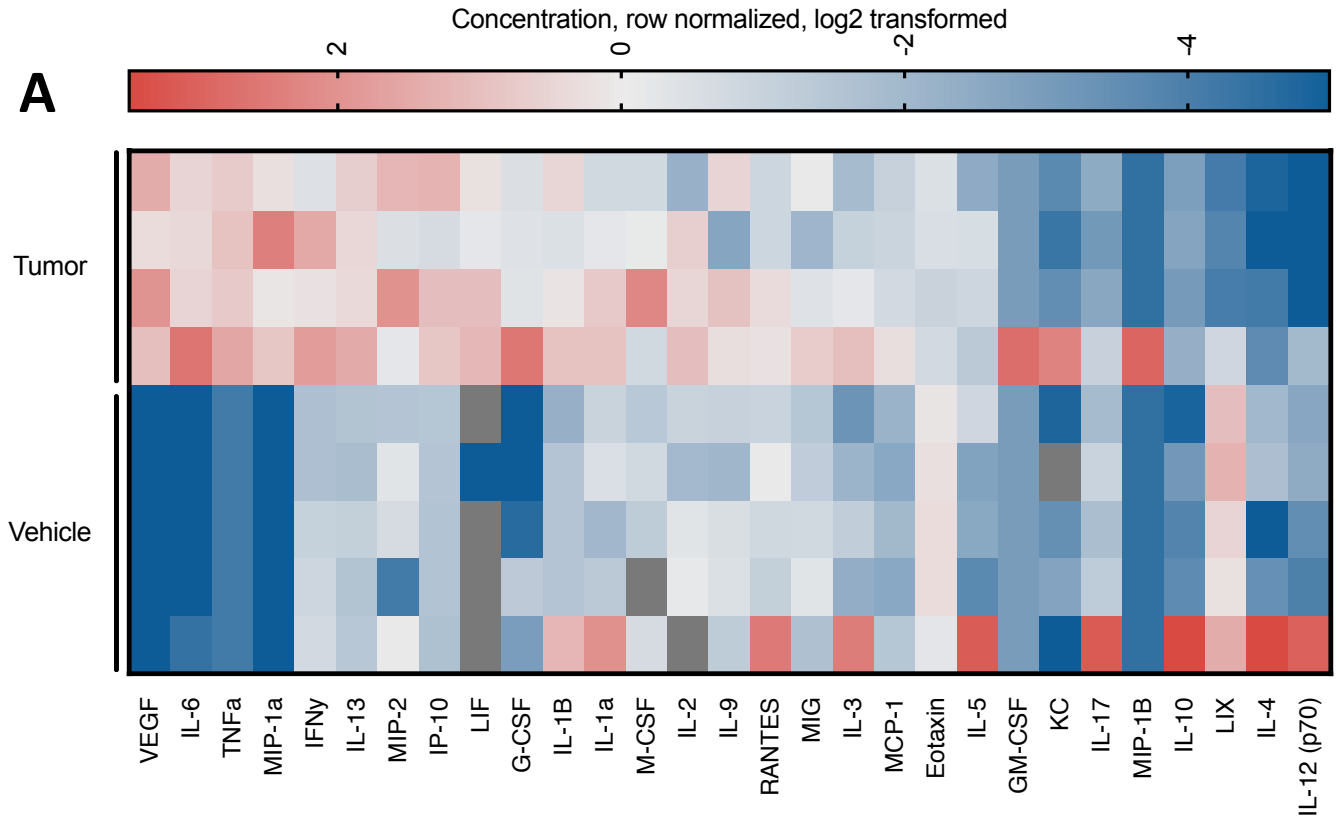
A
Concentration, row normalized, log2 transformed
2
0
-2
-4
Tumor
Vehicle
VEGF
IL-6
TNFa
MIP-1a
IFNy
IL-13
MIP-2
IP-10
LIF
G-CSF
IL-1B
IL-1a
M-CSF
IL-2
IL-9
RANTES
MIG
IL-3
MCP-1
Eotaxin
IL-5
GM-CSF
KC
IL-17
MIP-1B
IL-10
LIX
IL-4
IL-12 (p70)

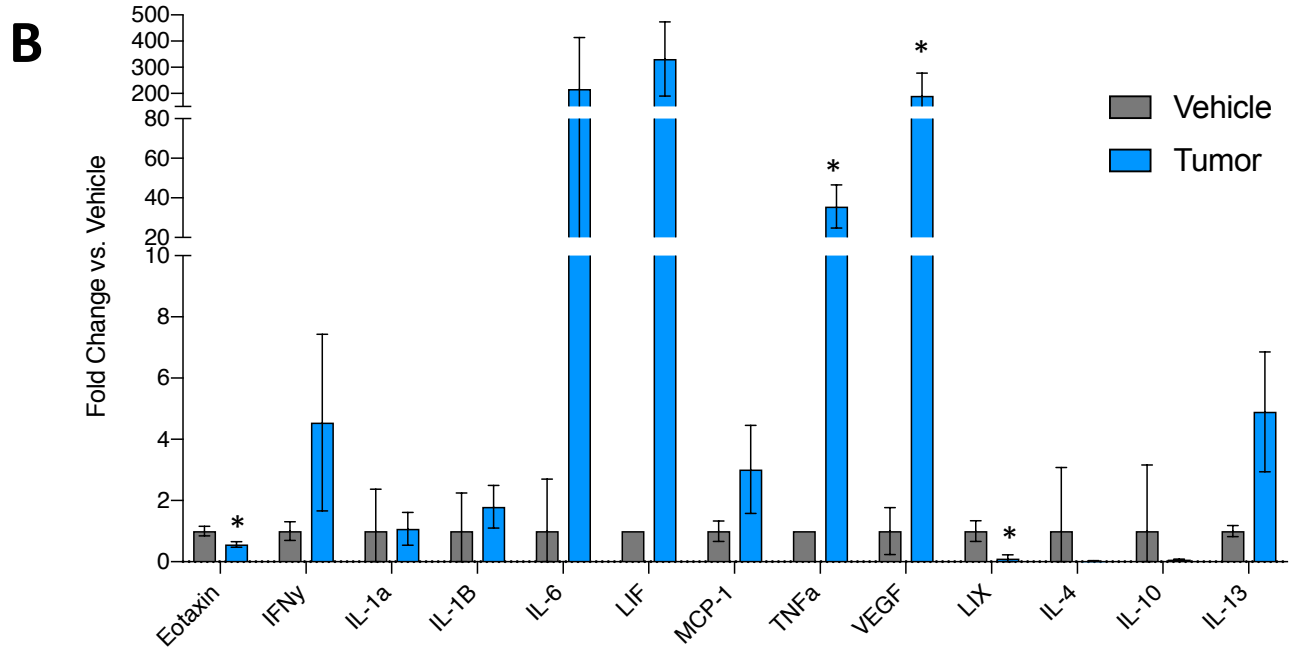
B
Fold Change vs. Vehicle
500
400
300
200
80
60
40
20
10
8
6
4
2
0
Vehicle
Tumor
*
Eotaxin
IFNy
IL-1a
IL-1B
IL-6
LIF
MCP-1
TNFa
VEGF
LIX
IL-4
IL-10
IL-13

Figure 3

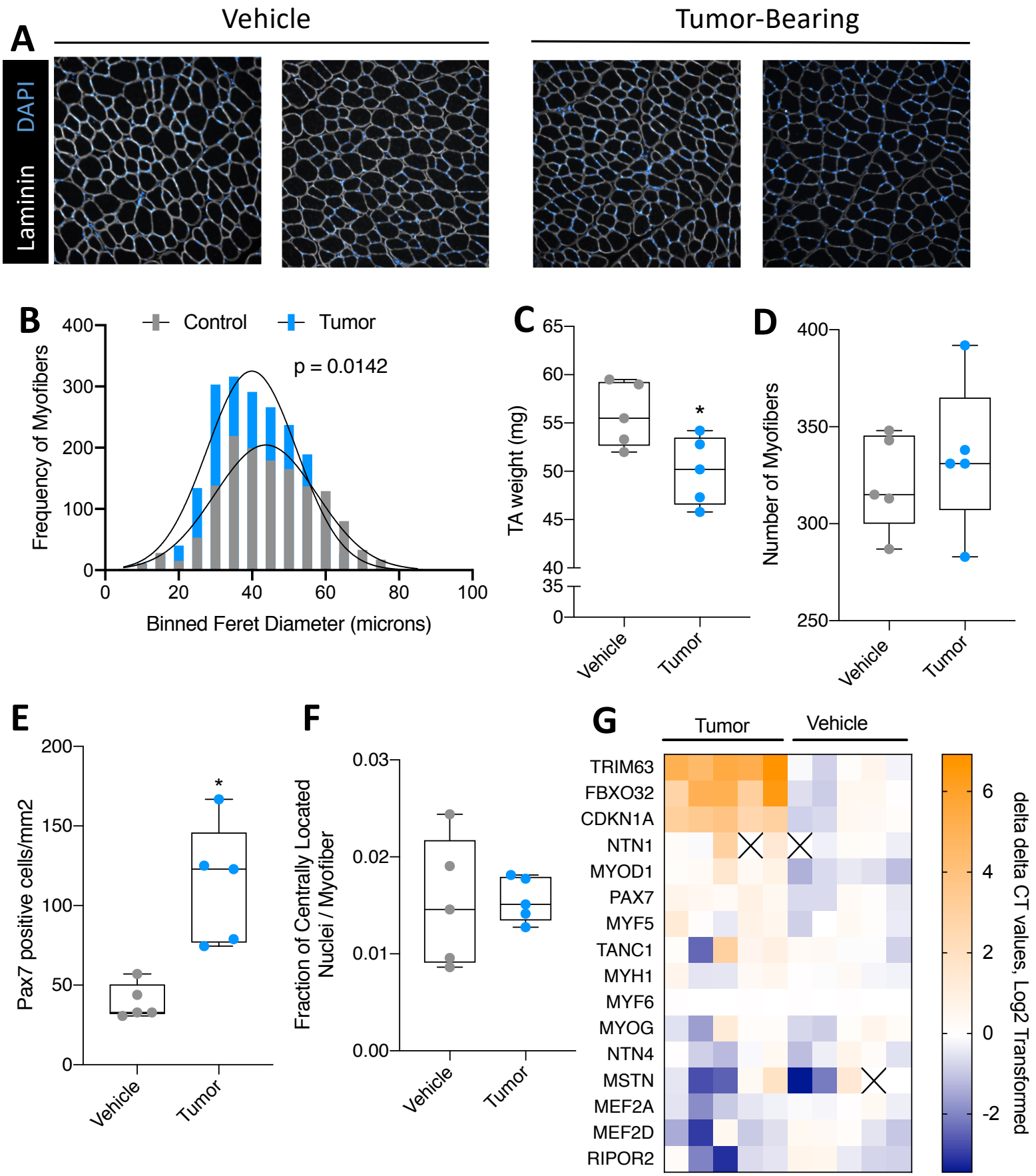
A
Vehicle
Tumor-Bearing
DAPI
Laminin
B
Control
Tumor
p = 0.0142
Frequency of Myofibers
Binned Feret Diameter (microns)
C
TA weight (mg)
Vehicle
Tumor
D
Number of Myofibers
Vehicle
Tumor
E
Pax7 positive cells/mm2
Vehicle
Tumor
F
Fraction of Centrally Located Nuclei / Myofiber
Vehicle
Tumor
G
Tumor
Vehicle
TRIM63
FBXO32
CDKN1A
NTN1
MYOD1
PAX7
MYF5
TANC1
MYH1
MYF6
MYOG
NTN4
MSTN
MEF2A
MEF2D
RIPOR2
delta delta CT values, Log2 Transformed

Figure 4

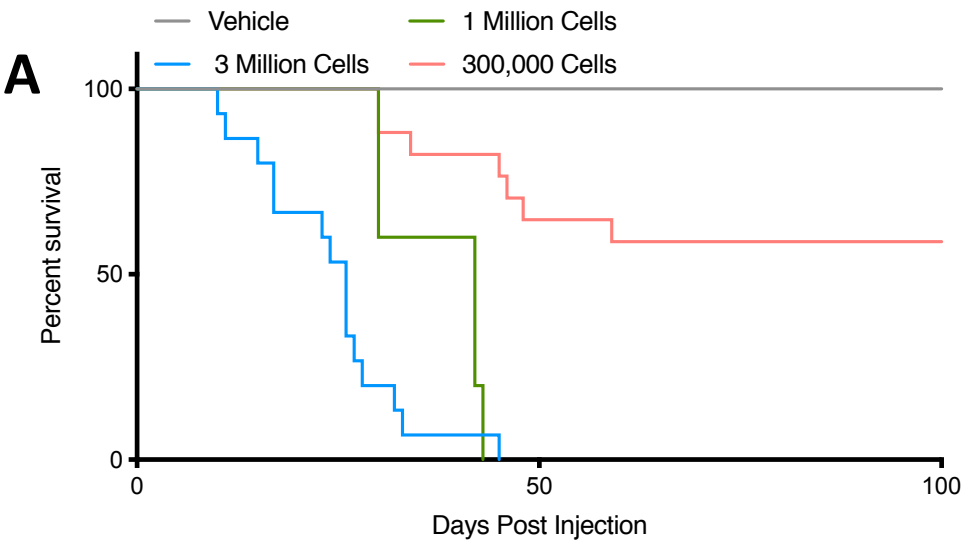

B

Cells Implanted	Median Survival (Days)
Vehicle	No Deaths
3 Million Cells	26
1 Million Cells	42
300,000 Cells	107

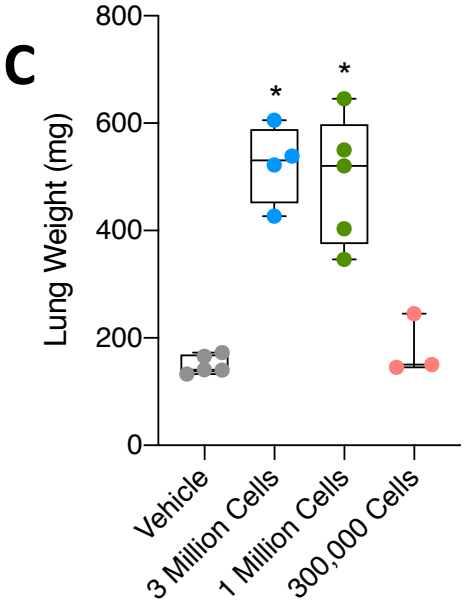

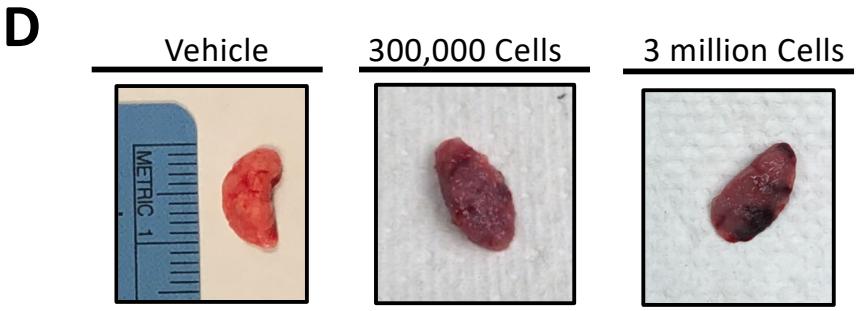

Figure 5

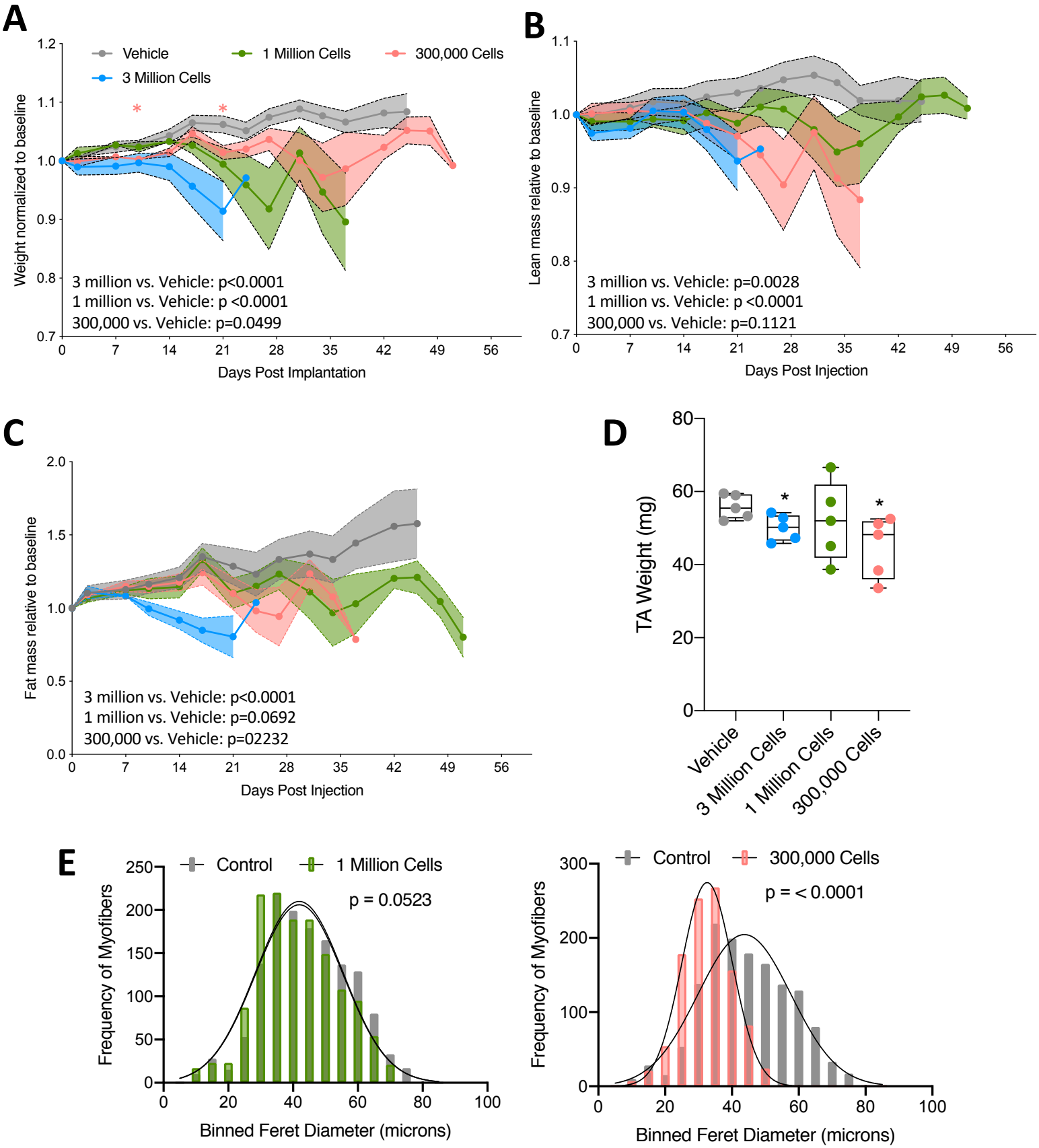
A
Vehicle
1 Million Cells
300,000 Cells
3 Million Cells
Weight normalized to baseline
3 million vs. Vehicle: p<0.0001
1 million vs. Vehicle: p <0.0001
300,000 vs. Vehicle: p=0.0499
Days Post Implantation
B
Lean mass relative to baseline
3 million vs. Vehicle: p=0.0028
1 million vs. Vehicle: p <0.0001
300,000 vs. Vehicle: p=0.1121
Days Post Injection
C
Fat mass relative to baseline
3 million vs. Vehicle: p<0.0001
1 million vs. Vehicle: p=0.0692
300,000 vs. Vehicle: p=02232
Days Post Injection
D
TA Weight (mg)
Vehicle
3 Million Cells
1 Million Cells
300,000 Cells
E
Control
1 Million Cells
p = 0.0523
Frequency of Myofibers
Binned Feret Diameter (microns)
Control
300,000 Cells
p = < 0.0001
Frequency of Myofibers
Binned Feret Diameter (microns)

Table 1

Group	% with Lung Tumor	% with Other Tumors	% with Metastasis in Thoracic Cavity
3,000,000 (n=15)	93	33 lower back 10 hindlimb	73
1,000,000 (n=5)	100	100	100
300,000 (n=15)	67	33 lower back	53
Vehicle (n=10)	0	0	0